Applied Acoustics 256 (2027) 111545

Contents lists available at ScienceDirect

Applied Acoustics

journal homepage: www.elsevier.com/locate/apacoust

Influence of installation and humidity conditions on the sound absorption coefficient of aeronautical glass wool: An experimental and machine-learning-based study

Alfonso Caiazzo [a,*], Giuseppe Petrone [a], Alessandro Casaburo [a], Immacolata Climaco [b], Aurelio Bifulco [b]

[a] PASTA LAB – Laboratory for Promoting Experiences in Aeronautical Structures and Acoustics, Department of Industrial Engineering, University of Naples Federico II, Naples, Italy

[b] Department of Chemical, Materials and Production Engineering (DICMaPI), University of Naples Federico II, Naples, Italy

HIGHLIGHTS

- The proposed framework identifies factors governing sound absorption variability.
- Humidity and protective layers strongly affect frequency-dependent response.
- Installation effects are negligible under controlled mounting conditions.
- Humidity sensitivity concentrates in three distinct frequency bands.

ARTICLE INFO

Dataset link: DATASET 1: Impedance Tube Installation and Environmental Variability Dataset (Original data)

Keywords:
Porous acoustic materials
Sound absorption coefficient
Aircraft insulation
Environmental effects
Installation effects
Supervised machine learning

ABSTRACT

Porous materials such as glass wool are widely used in aircraft fuselage insulation systems for their sound absorption performance. In operational aeronautical environments, their acoustic performance may differ from that measured under nominal laboratory conditions due to several factors such as protective coverings, installation procedures and moisture variations occurring during flight operations and throughout the aircraft service life. Despite their practical relevance, the effects of these non-nominal conditions on sound absorption variability remain insufficiently characterized. This study investigates the frequency-dependent sound absorption coefficient of aeronautical glass wools under controlled non-nominal conditions by combining impedance tube measurements, machine-learning techniques and Shapley additive explanations (SHAP). The investigated factors include material type, protective layers, relative humidity, humidity cycling and both controlled and operator-dependent mounting configurations. Results indicate that material, layer, relative humidity and humidity cycling significantly influence the acoustic response, with moisture-related effects exhibiting a strongly frequency-dependent behavior concentrated within three distinct frequency bands. Installation-related effects are also found to produce identifiable spectral variations, with operator-dependent mounting conditions generally associated with higher absorption levels and shifts of the peak response toward lower frequencies. The results further indicate that more controlled and uniformly distributed contact conditions improve measurement repeatability and reduce installation-induced variability.

1. Introduction

Noise reduction remains a critical requirement in modern aircraft design, as acoustic comfort directly affects passenger well-being and crew performance [1]. In pressurized fuselage structures, interior noise mitigation relies on fibrous porous absorbers integrated within the lining system. Conventional insulation packages using materials such as glass wool are widely employed in civil aircraft structural interiors due to their favorable acoustic and fire protection performance [2]. In aircraft applications, low-density glass-wool blankets are commonly enclosed within thin not acoustically neutral flexible polymeric covering films.

* Corresponding author.
Email address: alfonso.caiazzo@unina.it (A. Caiazzo).

https://doi.org/10.1016/j.apacoust.2026.111545
Received 8 June 2026; Received in revised form 6 August 2026; Accepted 27 August 2026
Available online 1 September 2026

These films form the thermal/acoustic insulation blanket assembly: they contain the glass fibers, provide a lightweight barrier against moisture ingress and contribute to compliance with the applicable flammability requirements [2–4]. For clarity and consistency, this covering film is hereafter referred to as the *protective layer*. Its finite surface mass and mechanical response, introduce an additional surface impedance at the air/glass wool interface and can therefore modify the sound absorption of the insulation package. The acoustic response is also sensitive to installation-induced compression, which locally changes the thickness and apparent density and may consequently alter its effective airflow resistivity.

While the acoustic properties of fibrous materials such as glass wool have been characterized under controlled and nominal conditions, discrepancies between predicted performance and actual in-service behavior are less documented. Petrone et al. [5] demonstrated that compression of fibrous blankets during mounting alters thickness and flow resistivity, potentially affecting the sound absorption coefficient, particularly in the low frequency region. Furthermore, experimental studies on porous absorbers indicate that geometric features and edge effects may influence absorption performance [6]. In parallel, data-driven analyses suggest that impedance tube measurements may be affected by operator-dependent variability during specimen installation [7,8]. To reduce such variability, Koruk proposed the use of a dedicated mounting fixture aimed at improving installation repeatability across different operators [9]. In particular, it has not yet been established whether the variability reported in the literature primarily originates from uncontrolled operator-dependent actions or from systematic differences in the local mechanical boundary conditions introduced during installation. The present work tackles this aspect through a repeatable experimental framework, designed to contrast controlled, fixture-based mounting conditions with realistic, operator-driven manual installations. In particular, the proposed framework isolates and quantifies the variability associated with the investigated installation configurations under representative operational conditions, enabling the identification of the mounting methodology that ensures the highest measurement repeatability and the lowest installation-induced variability.

Installation conditions, however, are not the only source of deviation from nominal acoustic behavior. Environmental exposure during service can also modify the physical state of fibrous insulation materials and consequently affect their acoustic response. Although the protective layer limits direct moisture exposure, it does not make the assembled insulation blanket hermetically sealed. Moisture ingress may occur through the finite vapor permeance of the film, seams, edges, penetrations, or localized damage, while temperature gradients can promote condensation within the blanket assembly. These mechanisms may result in gradual moisture accumulation in the porous glass-wool core [10]. Investigations into moisture resistance treatments for glass and mineral wool show that exposure to humidity can materially alter thermal properties [11]. Detailed absorption studies on glass wool products have quantified water vapor uptake over a wide range of relative humidities [12]. Yilmazer et al. show that moisture can affect the acoustic performance of fibrous materials, with the mid-to-high frequency range being the most sensitive [13]. In operational aeronautical environments, glass wool insulation systems are also subjected to repeated humidity fluctuations associated with successive flight phases, including ground operations, climb, cruise and descent. These variations may induce cyclic moisture absorption and desorption within the porous structure, potentially contributing to changes in acoustic behavior over time. Yet, the influence of humidity level and cyclic moisture exposure on the acoustic absorption of different glass wool materials has not been systematically investigated, particularly under operational mounting conditions including protective layers.

The combined effects of installation conditions, protective layers and environmental exposure generate complex and frequency-dependent variations in the measured sound absorption coefficient. Since these effects may overlap across the frequency domain, identifying the physical condition responsible for the observed acoustic response is not straightforward through conventional curve-by-curve comparisons. Recent studies have therefore investigated intelligent inverse-identification methods in which measured spectral responses are used to recover underlying structural, boundary or material parameters. Zhao et al. [14] combined an improved Fourier-series formulation with a particle-swarm-optimized back-propagation neural network to identify the boundary-supporting stiffness of flexible beams from their natural frequencies. Du et al. [15] subsequently employed a boundary-smoothed Fourier-series method coupled with a back-propagation neural network to identify the acoustic boundary impedance of enclosed cavities from modal-frequency data. In the field of porous-material characterization, Casaburo et al. [16] proposed a hierarchical ANN procedure to estimate the Johnson-Champoux-Allard parameters from specimen thickness and sound absorption data. These studies demonstrate the capability of intelligent methods to extract latent physical information from measured acoustic or structural spectra. However, previous inverse-identification approaches have primarily focused on estimating continuous model parameters under prescribed configurations, whereas the identification of the non-nominal installation and environmental conditions responsible for variations in the complete sound absorption spectrum remains unexplored. Accordingly, the scientific contribution of this work lies in the unified treatment of installation and moisture related variability within a single experimental framework. In contrast to previous investigations addressing individual mounting or environmental effects, or estimating continuous boundary and material parameters, the present approach uses sound absorption coefficient curves to distinguish categorical non-nominal conditions and identify their most informative frequency regions.

The objective of this work is therefore to determine whether the investigated material, installation and humidity conditions leave distinguishable signatures in the sound absorption response of aeronautical glass wool systems. Since each measured sound absorption coefficient curve is associated with categorical labels defined a priori by the controlled experimental conditions, the problem is formulated as a supervised classification task to assess whether these conditions can be recovered from the acoustic response [7,17]. In contrast, unsupervised methods would identify groupings driven by the dominant spectral variability, which need not correspond to the prescribed experimental factors. Classification accuracy is employed to assess the detectability of these acoustic signatures, whereas SHAP values are used to identify the frequency regions contributing most strongly to each classification. Two datasets are used to investigate variability in sound absorption measurements: (i) the *Installation and Environmental Variability Dataset*, $\mathcal{D}_1$, capturing the effects of material type, protective layers, installation procedures and humidity exposure; and (ii) the *Humidity Cycling Degradation Dataset*, $\mathcal{D}_2$, describing the evolution of the sound absorption coefficient under repeated humidity cycles. Given the high dimensionality of the datasets and the complex nonlinear interactions among the physical features, isolating the effect of individual variables from the frequency-dependent absorption curves is challenging. Rather than reproducing the full operational aircraft environment, the proposed framework aims to experimentally generate representative non-nominal conditions and evaluate whether the corresponding acoustic signatures can be discriminated through data-driven methods. Machine learning methods are therefore employed as qualitative discriminators to identify the features most strongly associated with variations in the absorption behavior, while SHAP values are used to quantify the frequency-dependent contribution of each feature. The proposed framework is based on an artificial neural network (ANN) methodology trained on the available experimental datasets. Although the results presented in this work are specific to the investigated dataset, the methodology itself is not restricted to it. To assess its generalization, the same ANN architecture and training procedure were applied to independent datasets available in the literature, yielding classification accuracies consistent with previously published results. This agreement indicates that the proposed framework can be extended to different parameters through progressive dataset enrichment while preserving its capability to identify the physical factors governing sound absorption variability.

The paper is organized as follows. Section 2 describes the experimental methodology adopted to perform the impedance tube measurements, including the controlled mounting conditions, the specimen humidification procedure and the preliminary analyses conducted on the measured sound absorption data. Section 3 introduces the machine learning framework used to analyze the datasets. In particular, it presents the description and preparation of datasets $\mathcal{D}_1$ and $\mathcal{D}_2$ and the artificial neural network (ANN) methods employed for both *univariate* and *multivariate* analyses. Section 4 reports the results of the classification analysis and the explainability assessment. Finally, Section 5 summarizes the main findings of the study and outlines possible directions for future work.

2. Experimental methodology

This section presents the experimental methodology adopted to generate the sound absorption curves investigated in this study, including the tested materials and protective layer, the humidity conditioning, the specimen mounting procedures and the acoustic measurement setup. The section is organized as follows. The Section 2.1 describes the materials, specimens, and protective layer. The humidity conditioning and cycling procedures are presented in Section 2.2, followed by the controlled and manual mounting procedures in Section 2.3. Finally, Section 2.4 describes the impedance tube setup and the selected operating frequency range. The complete experimental workflow, from specimen collection to acoustic measurement is summarized in Fig. 1. It comprises an initial specimen collection stage, followed by test preparation, during which the specimens are divided into the two datasets considered in this study. The subsequent stages include specimen conditioning, mounting, and experimental acoustic measurements using an impedance tube.

2.1. Materials, specimens, and protective layer

The specimens were supplied by GEVEN S.p.A. and prepared from Johns Manville Microlite® AA glass-wool blankets intended for aircraft thermal and acoustic insulation. Two material variants have been investigated: the commercial *Green* grade and the low-density *Grey* one. Both materials consist of resin-bonded borosilicate 902 biosoluble glass fiber. Table 1 reports the nominal apparent densities and the corresponding thermal conductivities at a mean temperature of 24°C for the two materials [18].

Table 1
Physical and thermal properties of the glass wool materials [18].

Materials	Density (kg/m^3)	Thermal conductivity at 24 °C (W/mK)
Green glass wool	9.6	0.036
Grey glass wool	6.7	0.040

GEVEN S.p.A. supplied the specimens in two configurations: uncovered glass wool and glass wool provided with a protective layer. The latter consisted of LAMAGUARD® 400 HR, a transparent, non-metallized, scrim-reinforced ethylene chlorotrifluoroethylene (ECTFE) covering film developed as a lightweight moisture barrier for aircraft thermal and acoustic insulation blankets [19]. The product weight comprises between 29.8 and 33.9 g/m^2, in compliance with FAR 25.856-a and BMS 8–377 Types 1 and 2. Specimens without and with the protective layer had average thicknesses of 20 mm and 10 mm, respectively [18]. The comparison between specimens with and without the protective layer has been performed to evaluate its influence on the measured normal-incidence sound absorption coefficient.

2.2. Humidity conditioning and cycling procedures

A controlled humidification process is implemented to condition the specimens at predefined relative humidity levels prior to acoustic testing. In accordance with Y. Ando & K. Kosaka [20], the procedure is carried out using a glove box (MBRAUN, type GB 2202-S), in which the specimens, auxiliary handling materials and silica gel used as a desiccator are placed. The enclosed and actively regulated volume enables stable humidity and temperature conditions, providing a controlled environment for specimen conditioning, similar to the functionality of a climatic chamber [10,13].

Relative humidity control is achieved by regulating the internal atmosphere of the glove box through the injection of dry nitrogen, allowing the target humidity level to be reached and maintained at a controlled temperature between 21 °C and 22 °C to minimize undesired fluctuations in relative humidity during the conditioning process. Once the desired relative humidity is stabilized, each specimen is kept inside the glove box under constant environmental conditions for a conditioning period of 24 h. The conditioning duration has been selected as a

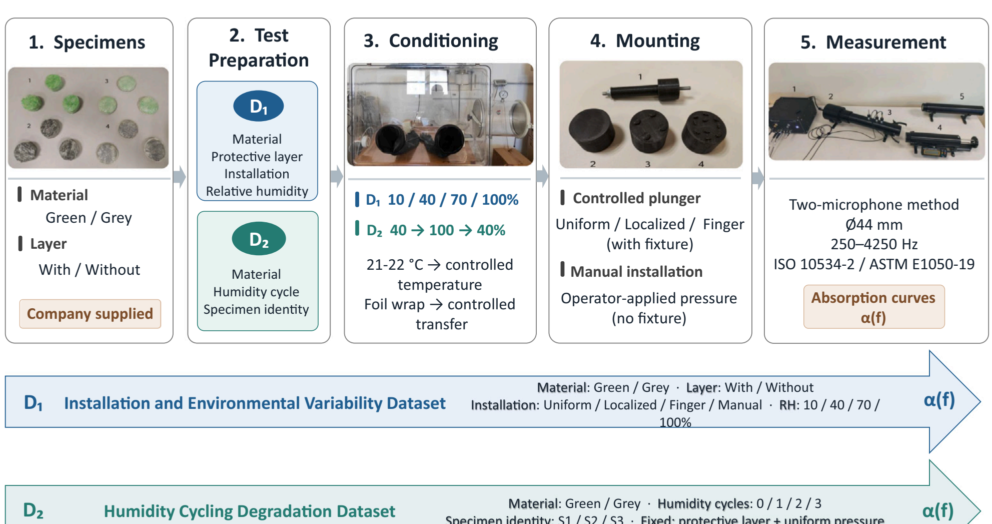

Fig. 1. Overview of the experimental workflow adopted to generate the sound absorption curves included in datasets $\mathcal{D}_1$ and $\mathcal{D}_2$.

practical compromise between moisture equilibration and experimental feasibility. For the conditioning stage at 100% RH, the objective is to promote moisture uptake under controlled atmospheric conditions, without direct contact with liquid water and minimizing the occurrence of condensation phenomena. After conditioning, the specimens are packaged in aluminum foil to minimize moisture exchange with the ambient environment and subsequently transferred to a desiccator containing moisture-buffering materials in order to limit unintended humidity variations during transportation to the impedance tube.

2.3. Specimen mounting procedures

Following the observations of Koruk [9], the mounting procedure is recognized as a potential source of variability in impedance tube measurements. Excessive insertion forces may locally alter the microstructure of porous materials, whereas insufficient forces may promote unintended air gaps between the specimen and the rigid plunger termination. In addition, Stender et al. [7,21] demonstrated that significant variations in the measured sound absorption coefficient may arise when nominally identical mounting procedures are performed by different operators.

To investigate these effects under repeatable and parametrically defined mounting conditions, a dedicated mounting fixture was designed and manufactured. The proposed approach follows the recommendation of Koruk [9] regarding the use of a plunger-based mounting system to reduce uncontrolled installation variability. All fixture components were first modeled using computer-aided design (CAD) software and subsequently fabricated in polylactic acid (PLA) using fused deposition modeling (FDM) 3D printing.

The fixture is based on a plunger equipped with three interchangeable terminations, as illustrated in Fig. 2. Each termination produces a different contact condition at the interface with the specimen, leading to repeatable variations in the spatial distribution of contact areas during installation. This setup makes it possible to evaluate in a systematic way whether a plunger-based mounting approach remains reliable under varying contact conditions, or if uncertainties similar to those highlighted by Stender et al. [7] can still occur. Alongside the fixture-based configurations, a manual installation case is also examined. In this scenario, the specimen is positioned and pressed without any dedicated device, allowing operator-dependent effects to emerge under realistic handling conditions. This combined approach enables a direct comparison between controlled and manual procedures, while also providing an internal evaluation of the variability associated with the different plunger terminations.

Three mounting conditions are investigated (Fig. 2, elements 2–4):

1. *Uniform pressure configuration*, featuring a flat termination that applies a spatially homogeneous load;

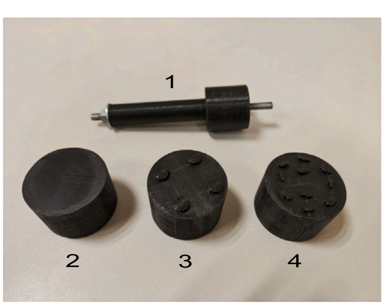

Fig. 2. Mounting fixture designed to ensure controlled and repeatable specimen installation in the impedance tube. The system enables different boundary conditions through: (1) plunger, (2) uniform pressure termination, (3) localized pressure termination and (4) finger pressure termination.

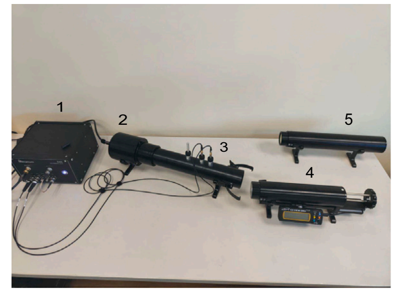

Fig. 3. Impedance tube setup based on the two-microphone method: (1) data acquisition system (DAQ), (2) loudspeaker, (3) microphones, (4) sample holder, and (5) anechoic termination.

2. *Localized pressure configuration*, with four circumferentially spaced cylinders applying discrete contact forces at fixed locations;
3. *Finger pressure configuration*, designed to reproduce, in a repeatable and geometrically defined manner, the non-uniform and spatially distributed contact patterns typically generated by operator handling during specimen installation. To achieve this, the geometry of human fingertips was reconstructed through a photogrammetry-based procedure: ten photographs of each of the five fingertips were acquired from multiple viewing angles and processed to generate a three-dimensional point cloud. The resulting reconstruction was then converted into a solid 3D model, imported into the CAD environment, scaled and used to define the contact geometry of the finger pressure termination in a fully controlled and repeatable manner.

In parallel to the fixture-based configurations, the *manual installation* condition is performed by direct operator-applied pressure without the use of the mounting fixture, in order to provide a reference case representative of unconstrained installation practice. This enables the assessment of whether the use of a repeatable fixture-based mounting system effectively reduces variability not only across different termination geometries, but also with respect to standard manual handling.

2.4. Impedance tube setup

The normal-incidence sound absorption coefficient, $\alpha(f)$, has been measured using the two-microphone method in accordance with ISO 10534-2 [22] and ASTM E1050-19 [23]. The experimental setup, shown in Fig. 3, comprises a data acquisition system, a loudspeaker, two microphones, a sample holder, and an anechoic termination. The tube has a circular cross-section with an inner diameter of 44 mm, while the two microphones are separated by a distance of 30 mm.

The operating frequency range of an impedance tube is constrained by both the microphone spacing and the onset of non-planar acoustic modes. Following the criteria reported in ISO 10534-2 [22], the lower and upper frequency limits can be expressed as:

$$f_1 > 0.015\frac{c_0}{s}, \qquad f_u < \min\left(0.45\frac{c_0}{s}, 0.58\frac{c_0}{d}\right) \tag{1}$$

where c_0 is the speed of sound in the tube, s is the microphone spacing, and d is the inner diameter of the tube. The nominal usable range extends from approximately 170 Hz to 4487 Hz. A preliminary inspection of the measured absorption curves revealed reduced repeatability and spurious oscillations close to the lower and upper theoretical operating limits. Therefore, all subsequent analyses have been restricted to the stable frequency range 250-4250 Hz.

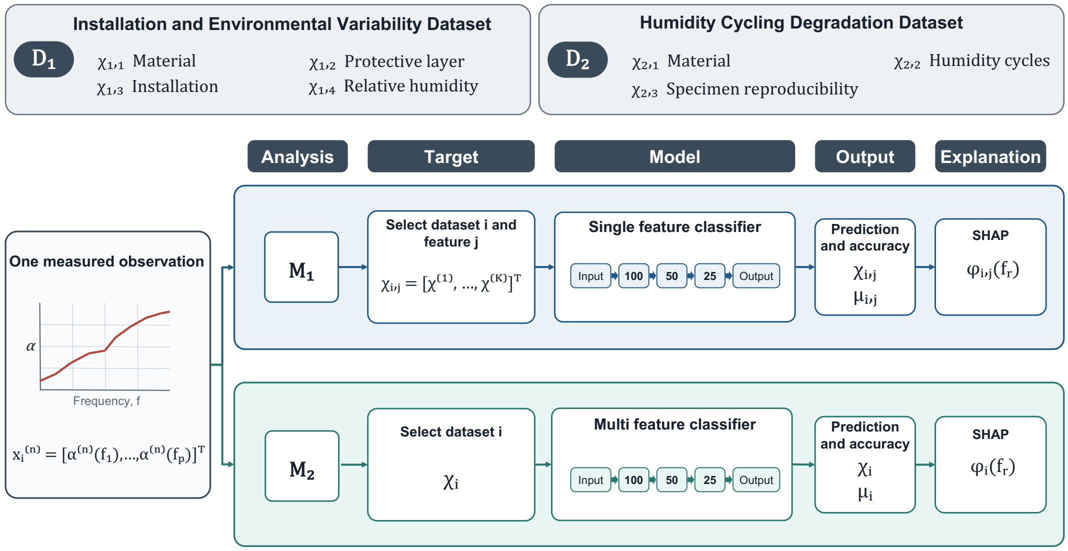

Fig. 4. Workflow for analyzing the n-th sound absorption coefficient curve selected from the dataset $\mathcal{D}_i$, with $i \in \{1, 2\}$, through *univariate* and *multivariate* classification and SHAP-based interpretation.

3. Machine learning approaches

This section presents the machine learning framework used to analyze the acoustic absorption datasets. It begins with the description and preparation of datasets $\mathcal{D}_1$ and $\mathcal{D}_2$ (Sections 3.1, 3.2). It is followed by the introduction of the artificial neural network (ANN) methods for both *univariate* and *multivariate* analyses (Section 3.3). Finally, the description of the explainability analysis based on SHAP values (Section 3.4). The complete data-analysis workflow, from the experimental sound absorption curves to the interpretation of the model predictions is summarized in Fig. 4. It comprises an initial data preparation stage, during which the curves are processed and divided into training, validation, and test subsets. The subsequent stages include ANN training through the *univariate* and *multivariate* approaches, evaluation of model performance in terms of classification accuracy and loss, and SHAP-based analysis of the model predictions.

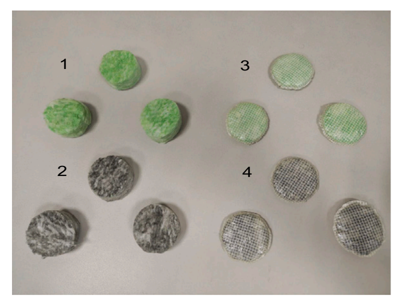

Fig. 5. Glass wool specimens investigated in this study: (1) green glass wool without a protective layer, (2) grey glass wool without a protective layer, (3) green glass wool with a protective layer and (4) grey glass wool with a protective layer.

3.1. Dataset description

Two distinct datasets are considered, each addressing a different aspect of acoustic variability and degradation. The *Installation and Environmental Variability Dataset* $\mathcal{D}_1$ is composed of 648 measurements and its design, aims to assess the influence of material type, protective layer, mounting configuration and humidity level across the frequency domain. Three nominally identical specimens are tested for each material–protective layer combination, resulting in a total of 12 specimens (see Fig. 5).

The investigated features for dataset $\mathcal{D}_1$ are:

- **Material** $\chi_{1,1}$**:** Two aeronautical glass wool sound absorber materials with a nominal thickness of $t = 20$ mm, are investigated. The materials differ in fiber density and micro-structural compaction, resulting in different airflow resistivity while maintaining comparable macroscopic geometry.
- **Protective layer** $\chi_{1,2}$**:** Each material is tested both with and without the protective layer.
- **Installation** $\chi_{1,3}$**:** Four installation conditions are investigated. Three fixture-based configurations are implemented through a plunger mounting system characterized by different contact pressure distributions at the specimen interface: (i) *uniform pressure*, (ii) *local pressure* and (iii) *finger pressure*. In addition, a fourth condition, denoted as *manual pressure*, reproduces direct operator-dependent specimen installation without the use of the plunger-based fixture.
- **Relative humidity** $\chi_{1,4}$**:** Four controlled humidity levels, selected to span from dry conditions to full saturation, are considered: 10%, 40%, 70% and 100% relative humidity (RH).

The *Humidity Cycling Degradation Dataset* $\mathcal{D}_2$ is conceived to investigate the progressive degradation of the acoustic absorption performance induced by repeated exposure to moisture. The dataset consists of 90 impedance tube measurements and is restricted to specimens equipped with the protective layer and the uniform pressure configuration. The experimental design of $\mathcal{D}_2$ aims to isolate the effects of material properties, cyclic humidity exposure and specimen-to-specimen variability on the measured sound absorption coefficient across the frequency domain. The investigated features for dataset $\mathcal{D}_2$ are:

- **Material** $\chi_{2,1}$**:** The same two aeronautical glass wool sound absorber materials introduced in dataset $\mathcal{D}_1$ are considered.
- **Humidity cycles** $\chi_{2,2}$**:** The controlled humidity sequence is intended to reproduce representative operational moisture variations through three consecutive stages: initial conditioning at 40% relative humidity (RH), subsequent exposure to saturated conditions (100% RH) until hygroscopic equilibrium is approached and final reconditioning at 40% RH prior to acoustic testing. The sequence

Table 2
Categorical features and corresponding values for datasets $\mathcal{D}_1$ and $\mathcal{D}_2$.

Dataset	Feature	Values
$\mathcal{D}_1$	Material	Green wool, Grey wool
	Protective layer	With, Without
	Installation configuration	Uniform, Localized, Finger, Manual pressure
	Relative humidity	10%, 40%, 70%, 100%
$\mathcal{D}_2$	Material	Green wool, Grey wool
	Humidity cycles	0, 1, 2, 3
	Specimen identity	1, 2, 3

is repeated progressively in order to evaluate the effects of cyclic moisture exposure on the acoustic response of the investigated materials. A total of three humidity cycles are considered in the present study.

- **Specimen identity** $\chi_{2,3}$**:** To quantify the specimen-to-specimen variability, three nominally identical specimens are tested for each material configuration. As the dataset is centered on specimens with layers, a total of six specimens have been tested (three per material).

In the present study, the investigated features can be defined as categorical, since they are experimentally controlled variables that assume a finite set of discrete values, each treated as a distinct value in the machine learning framework. A summary of the investigated features and their values, for both datasets $\mathcal{D}_1$ and $\mathcal{D}_2$, can be found in Table 2.

3.2. Dataset preparation

Prior to training, the sound absorption coefficient curves are pre-processed following the procedure used by Stender et al. [7]. It includes, in order:

1. *Rolling-median smoothing* with a 25-sample window, is applied to attenuate random experimental variability, thereby limiting the risk that these fluctuations are learned as physically meaningful absorption features.
2. *Rolling-maximum smoothing* with a 50-sample window, is applied to preserve the dominant absorption envelope of the curves. This step ensures that physically meaningful features such as maximum and/or plateau regions are not attenuated during the process.
3. *Frequency-domain downsampling* by a factor of 5, is applied to reduce input dimensionality and mitigate overfitting. The reduction factor is selected by ensuring that the discrepancy between the smoothed and downsampled curves, evaluated at the common frequency points, remains below 1%.

Fig. 6 shows a random absorption coefficient curve from dataset $\mathcal{D}_1$ before and after the pre-processing procedure. As Fig. 6 shows, the smoothing operations only marginally modify the original curve while preserving its overall physical behavior. In addition, the downsampled curve remains perfectly superimposed on the smoothed one, confirming that the dimensionality reduction does not alter the relevant absorption features.

Each observation consists of one pre-processed sound absorption coefficient curve and the corresponding set of ground-truth categorical labels encoded using the one-hot encoding technique [24]. The resulting one-hot vector serves as the target label for the supervised machine learning methods. Each categorical feature (i.e., material, diameter, etc.) is represented by a separate sequence of 0 and 1 and all segments are concatenated into a single, ordered target vector. For dataset $\mathcal{D}_i$, each categorical feature $\chi_{i,j}$ is represented by a separate one-hot vector $\mathbf{y}_{i,j}^{(l)}$ of dimension $C_{i,j}$, where $C_{i,j}$ is the number of classes associated with that feature. For the *multivariate* method $\mathcal{M}_2$, the feature-specific vectors are

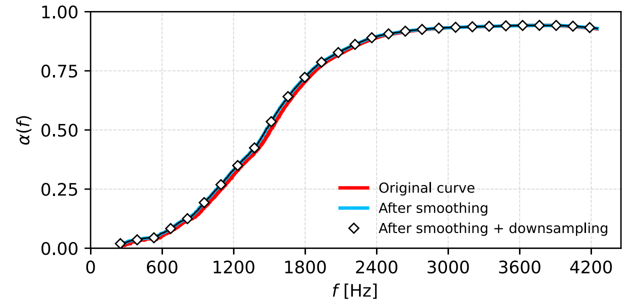

Fig. 6. Comparison between the original absorption coefficient curve, the smoothed curve and the smoothed downsampled curve for a random sample from dataset $\mathcal{D}_1$.

concatenated as $\mathbf{y}_i^{(l)} = [\mathbf{y}_{i,1}^{(l)\top}, \dots, \mathbf{y}_{i,J_i}^{(l)\top}]^\top$, where J_i is the total number of categorical features. Dataset $\mathcal{D}_1$ contains $J_1 = 4$ categorical features with respective dimensions $C_{1,1} = 2$, $C_{1,2} = 2$, $C_{1,3} = 4$ and $C_{1,4} = 4$, with an overall dimensionality of 12. Dataset $\mathcal{D}_2$ contains $J_2 = 3$ categorical features with dimensions $C_{2,1} = 2$, $C_{2,2} = 4$ and $C_{2,3} = 3$, resulting in a target-vector dimension of 9. For the *univariate* method $\mathcal{M}_1$, only the feature-specific segment $\mathbf{y}_{i,j}^{(l)}$ is used as the target, and the corresponding output dimension is therefore $C_{i,j}$. The values corresponding to each feature are listed in the third column of Table 2. Let's take for instance the absorption coefficient curve l, from dataset $\mathcal{D}_1$. The measurement has been taken with a green wool specimen (1,0) with the protective layer (1,0), employing the finger pressure configuration (0,0,1,0) and 70% of relative humidity (0,0,1,0). The one-hot encoded ground truth vector would read:

$$\mathbf{y}_1^{(l)} = [\underbrace{1,0}_{\chi_{1,1}}, \underbrace{1,0}_{\chi_{1,2}}, \underbrace{0,0,1,0}_{\chi_{1,3}}, \underbrace{0,0,1,0}_{\chi_{1,4}}]^\top \tag{2}$$

The collection of pre-processed input curves and corresponding target vectors defines the datasets used to train and evaluate the supervised machine learning methods presented in the following section.

3.3. Artificial neural networks

Two artificial neural network methods are employed to identify the categorical features encoded in the measured sound absorption coefficient curves. For the dataset $\mathcal{D}_i$, the l-th observation is represented by the frequency-domain vector defined as:

$$\mathbf{x}_i^{(l)} = \left[\alpha_i^{(l)}(f_1), \dots, \alpha_i^{(l)}(f_R)\right]^\top \tag{3}$$

where R is the total number of frequency points considered.

Both methods employ the same fully connected feedforward hidden architecture, selected to capture nonlinear frequency-domain relationships and to provide a controlled comparison between the *univariate* and *multivariate* formulations. This choice is consistent with previous ANN-based inverse classification of impedance tube measurements [7]. Neural networks were preferred over alternative supervised classifiers, such as k-Nearest Neighbors, Decision Trees, Linear Discriminant Analysis and Random Forests, since a comparable explainable-machine-learning study on impedance-tube sound absorption measurements reported neural networks among the best-performing algorithms for identifying the factors affecting the measured sound absorption coefficient, under both *univariate* and *multivariate* formulations [25].

The network consists of three hidden layers containing 98, 50 and 25 neurons, respectively. Denoting the input to the network by $\mathbf{h}^{(l,0)} = \mathbf{x}_i^{(l)}$, the forward propagation through a network with H hidden layers is expressed as

$$\mathbf{h}^{(l,q)} = \rho\left(\mathbf{W}^{(q)}\mathbf{h}^{(l,q-1)} + \mathbf{b}^{(q)}\right), \qquad q = 1, \dots, H \tag{4}$$

where $\mathbf{W}^{(q)}$ and $\mathbf{b}^{(q)}$ are the trainable weights and biases and $\rho(z) = \max(0, z)$ is the Rectified Linear Unit activation function.

Following the hidden-layer transformations defined in Eq. (4), the network output is calculated as:

$$\hat{\mathbf{y}}^{(l)} = \sigma\left(\mathbf{W}^{(H+1)}\mathbf{h}^{(l,H)} + \mathbf{b}^{(H+1)}\right), \qquad \sigma(z) = \frac{1}{1+\exp(-z)} \tag{5}$$

where the sigmoid activation provides an independent probability estimate for each output class.

On the one hand, the *univariate* method $\mathcal{M}_1$ predicts a single categorical feature $\chi_{i,j}$. Its output vector $\hat{\mathbf{y}}_{i,j}^{(l)}$ contains $C_{i,j}$ components, one for each class associated with the investigated feature. A separate network is therefore trained for each investigated feature (see Fig. 4). This formulation determines how strongly the values of an individual feature are encoded in the sound absorption coefficient curves.

On the other hand, the *multivariate* method $\mathcal{M}_2$ simultaneously predicts the values associated with all J_i features. This multi-output formulation allows the network to account for statistical relationships among the feature labels [26,27]. The hidden-layer architecture in Eq. (4) is retained to provide a controlled comparison with $\mathcal{M}_1$, while the output-layer dimension is adapted to the complete set of values.

For $\mathcal{M}_2$, the target and prediction vectors are obtained by concatenating the feature-specific one-hot encoded segments:

$$\mathbf{y}_i^{(l)} = \left[\mathbf{y}_{i,1}^{(l)\top}, \dots, \mathbf{y}_{i,J_i}^{(l)\top}\right]^\top, \qquad \hat{\mathbf{y}}_i^{(l)} = \left[\hat{\mathbf{y}}_{i,1}^{(l)\top}, \dots, \hat{\mathbf{y}}_{i,J_i}^{(l)\top}\right]^\top \tag{6}$$

Let $C_{i,j}$ denote the number of values associated with feature $\chi_{i,j}$. For the *univariate* method $\mathcal{M}_1$, a separate classifier is trained for each feature. Therefore, the classifier associated with feature $\chi_{i,j}$ contains $C_{i,j}$ output neurons. Its binary cross-entropy loss is defined as:

$$\mathcal{L}_{i,j}^{\mathcal{M}_1} = -\frac{1}{N_{\text{tr}}C_{i,j}} \sum_{l=1}^{N_{\text{tr}}} \sum_{k=1}^{C_{i,j}} \left[y_{i,j,k}^{(l)} \log \hat{y}_{i,j,k}^{(l)} + \left(1 - y_{i,j,k}^{(l)}\right) \log\left(1 - \hat{y}_{i,j,k}^{(l)}\right)\right] \tag{7}$$

where N_{tr} is the number of training observations, $y_{i,j,k}^{(l)}$ is the k-th binary component of the ground-truth segment $\mathbf{y}_{i,j}^{(l)}$ and $\hat{y}_{i,j,k}^{(l)}$ is the corresponding predicted output.

For the *multivariate* method $\mathcal{M}_2$, the output segments associated with the J_i features are concatenated, so that the total number of output neurons is $C_i = \sum_{j=1}^{J_i} C_{i,j}$. Accordingly, the binary cross-entropy loss is evaluated over the complete concatenated output vector, i.e., by extending the summation in Eq. (7) over all J_i features.

The network parameters are optimized using ADAM [28], with an initial learning rate of 10^{-3}, by minimizing Eq. (7) for $\mathcal{M}_1$, and its *multivariate* extension described above for $\mathcal{M}_2$. In the *multivariate* case, the output vector is subsequently partitioned into its feature-specific segments to evaluate the predictions associated with each feature independently. A batch size of 32 and a maximum of 500 training epochs are adopted for both methods.

To enable a direct comparison between the two methods, the *multivariate* output in Eq. (6) is partitioned into its feature-specific segments [29–31]. For both methods, the predicted class index for feature $\chi_{i,j}$ is obtained by applying the maximum-score criterion within the corresponding output segment:

$$\hat{c}_{i,j}^{(l)} = \arg\max_{k=1,\dots,C_{i,j}} \hat{y}_{i,j,k}^{(l)} \tag{8}$$

The predicted class index obtained from Eq. (8) is then compared with the corresponding ground-truth class index. The feature-specific classification accuracy is defined as

$$\mu_{i,j} = \frac{1}{N_{\text{te}}} \sum_{l=1}^{N_{\text{te}}} \mathbb{1}\left[\hat{c}_{i,j}^{(l)} = c_{i,j}^{(l)}\right] \tag{9}$$

where $c_{i,j}^{(l)}$ is the ground-truth class, N_{te} is the number of test observations and $\mathbb{1}[\cdot]$ denotes the indicator function. The segmentation procedure therefore provides one value of Eq. (9) for each feature predicted by $\mathcal{M}_2$, enabling direct comparison with the corresponding independent classification performed using $\mathcal{M}_1$.

Model performance is evaluated using a five-fold cross-validation procedure applied at the individual-curve level. The same folds are used for both $\mathcal{M}_1$ and $\mathcal{M}_2$. At each iteration, four folds, corresponding to 80% of the complete dataset, are used to optimize the network weights, whereas the remaining fold, corresponding to 20%, is held out and used exclusively for performance evaluation after training. No hyperparameter optimization, model selection, or validation-based early-stopping strategy has been performed. Rotating the test fold ensures that each observation is evaluated exactly once and reduces the dependence of the reported performance on a single data partition.

For each categorical feature, the classification accuracy defined in Eq. (9) and the macro-averaged F1 score are calculated for each test fold. The final performance is reported as the mean and standard deviation of both metrics across the five test folds.

3.4. Interpretation of classification methods

The present study employs SHAP values to quantify the contributions of individual frequency components to the classification of each categorical variable [32,33]. Frequencies serve as input features for the SHAP analyses, which are conducted for both the *univariate* ($\mathcal{M}_1$) and *multivariate* ($\mathcal{M}_2$) methods.

For the l-th sound absorption coefficient curve belonging to dataset $\mathcal{D}_i$, the network input is the vector $\mathbf{x}_i^{(l)}$ defined in Eq. (3). Its r-th component, $\alpha_i^{(l)}(f_r)$, is the absorption coefficient measured at frequency f_r, with $r = 1, \dots, R$.

For a selected categorical feature $\chi_{i,j}$ and one of its values $k = 1, \dots, C_{i,j}$, let $P_k(\mathbf{x}_i^{(l)})$ denote the probability assigned by the neural network to value k when the l-th sound absorption coefficient curve is provided as input.

Let $\mathcal{R} = \{1, \dots, R\}$ denote the complete set of frequency indices and let $\mathcal{S} \subseteq \mathcal{R} \setminus \{r\}$ be a subset that does not contain the frequency index r. The SHAP value associated with frequency f_r, curve l and value k is defined as

$$\phi_k^{(l)}(f_r) = \sum_{\mathcal{S} \subseteq \mathcal{R} \setminus \{r\}} \frac{|\mathcal{S}|!\,(R - |\mathcal{S}| - 1)!}{R!} \left[P_k^{(l)}(\mathcal{S} \cup \{r\}) - P_k^{(l)}(\mathcal{S})\right] \tag{10}$$

where $P_k^{(l)}(\mathcal{S})$ is the expected probability assigned to value k when the frequency components indexed by $\mathcal{S}$ are considered. The difference in square brackets therefore quantifies the change in the class-specific output produced by including the absorption coefficient at frequency f_r in the subset $\mathcal{S}$.

Since exact evaluation of Eq. (10) requires considering 2^{R-1} feature subsets, the KernelSHAP Python library [34] is employed to approximate the SHAP values via weighted sampling of these subsets.

The resulting SHAP values satisfy the additive decomposition

$$P_k\left(\mathbf{x}_i^{(l)}\right) = \mathbb{E}\left[P_k(\mathbf{X}_i)\right] + \sum_{r=1}^{R} \phi_k^{(l)}(f_r) \tag{11}$$

where $\mathbb{E}[P_k(\mathbf{X}_i)]$ is the class-specific baseline output estimated from the background data used by KernelSHAP.

The SHAP values are computed for each frequency and interpreted according to both sign and magnitude with respect to this expected value. Specifically, a *positive* SHAP value indicates that the observed absorption coefficient at frequency f_r increases the predicted probability of the corresponding value relative to the baseline in Eq. (11), whereas *negative* values indicate a decrease in the probability of detecting that class. SHAP values with magnitudes below 10^{-4} are considered negligible [7,35,36], indicating that the associated frequency carries minimal information for classification.

The formulation applies to both $\mathcal{M}_1$ and $\mathcal{M}_2$, since SHAP values are evaluated separately for each scalar value output. For $\mathcal{M}_2$, the relevant

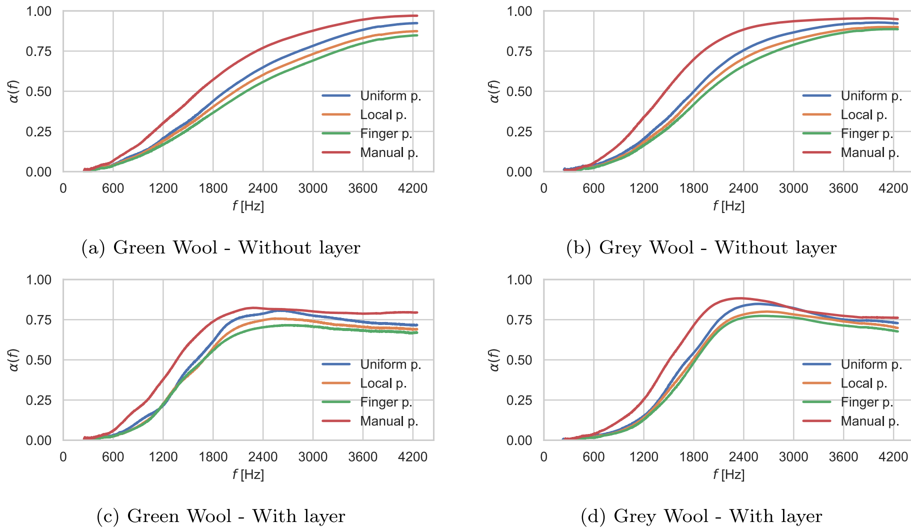

(a) Green Wool - Without layer (b) Grey Wool - Without layer

(c) Green Wool - With layer (d) Grey Wool - With layer

Fig. 7. Comparison of the effects of mounting conditions on the sound absorption coefficient. Each curve represents the average of 27 measurements.

value outputs are identified by partitioning the concatenated prediction vector into the feature-specific segments defined in Eq. (6).

To account for all the classes associated with the categorical feature $\chi_{i,j}$, the total absolute SHAP contribution [7] of frequency f_r for curve l is defined as:

$$\Phi_{i,j}^{(l)}(f_r) = \sum_{k=1}^{C_{i,j}} \left|\phi_k^{(l)}(f_r)\right| \tag{12}$$

where $C_{i,j}$ is the number of classes associated with the feature $\chi_{i,j}$. For a set of analyzed curves, the mean $\mu_{i,j}(f_r)$ and standard deviation $\sigma_{i,j}(f_r)$ of $\Phi_{i,j}^{(l)}(f_r)$ are computed to characterize the average contribution of each frequency and its variability across curves.

A frequency-domain reference level is introduced to identify the portions of the spectrum providing above-average information for classification. The threshold $\overline{\mu}_{i,j}$ corresponds to the average discriminative contribution over the entire investigated frequency range and provides an objective, data-driven reference level, avoiding the need for an arbitrarily chosen threshold. A similar mean-based thresholding criterion is commonly adopted in variable-importance-based feature selection [37], where a variable (or, in the present case, a frequency component) is retained as relevant when its importance score exceeds the average importance computed over the complete set of variables:

$$\overline{\mu}_{i,j} = \frac{1}{R}\sum_{r=1}^{R} \mu_{i,j}(f_r) \tag{13}$$

where R is the number of investigated frequency points. A frequency component is considered to provide above-average discriminative information when

$$\mu_{i,j}(f_r) > \overline{\mu}_{i,j} \tag{14}$$

4. Results

This section presents the results obtained by applying the previously described data-driven methods to the experimental datasets. Before considering the model predictions, the measured sound absorption coefficient curves are directly examined in Section 4.1 to identify the main trends associated with the investigated experimental conditions. This model-independent analysis reveals frequency-dependent variations and, in some cases, overlapping acoustic responses whose dependence on the individual experimental factors cannot be systematically assessed through direct visual comparison alone. These observations motivate the subsequent application of data-driven methods. The prediction outcomes of the *univariate* ($\mathcal{M}_1$) and *multivariate* ($\mathcal{M}_2$) methods, are used to perform a qualitative analysis: the achieved classification accuracy serves as a discriminant to determine whether a given feature significantly influences the sound absorption coefficient curves. A complementary quantitative analysis is then carried out using Shapley explanatory values (SHAP), which explain the contribution of each feature across the frequency spectrum, highlighting the frequency bands that are most sensitive to each feature. The experimental investigation of the acoustic response is presented in Section 4.1. The qualitative results are discussed separately for datasets $\mathcal{D}_1$ and $\mathcal{D}_2$ in Sections 4.2 and 4.3 respectively, while the explainability analysis for both datasets can be found in Section 4.4.

4.1. Analysis of the experimental results

Prior to the application of machine learning methods, a preliminary analysis is performed directly on the measured data for both datasets $\mathcal{D}_1$ and $\mathcal{D}_2$.

The *Installation and Environmental Variability Dataset* $\mathcal{D}_1$ contains sound absorption coefficient curves acquired for two glass wool materials, both with and without a protective layer. For each feature configuration, 27 repeated measurements were performed and subsequently averaged in order to reduce random measurement variability. The resulting averaged curves, shown in Figs. 7 and 8, provide a preliminary qualitative assessment of the effects of mounting conditions and relative humidity.

Fig. 7 illustrates the influence of four pressure conditions during mounting: uniform, localized, finger and manual pressure. The Fig. 4(a) and (b) correspond to specimens without the protective layer. Both materials exhibit a monotonic increase in the sound absorption coefficient with frequency. For all the investigated frequencies, the manual installation condition provides systematically higher absorption values than the plunger-based configurations. Among the plunger configurations, the *uniform pressure* termination exhibits the highest absorption coefficients, followed by the *localized pressure* and *finger pressure* terminations. For the plunger-mounted green wool, between the *uniform* and *finger pressure* configurations, the highest sound absorption coefficient variation reaches 16% in the frequency band 1800–4250 Hz. The corresponding 16% variation for grey wool can be seen in the narrowed 2000–2800 Hz band.

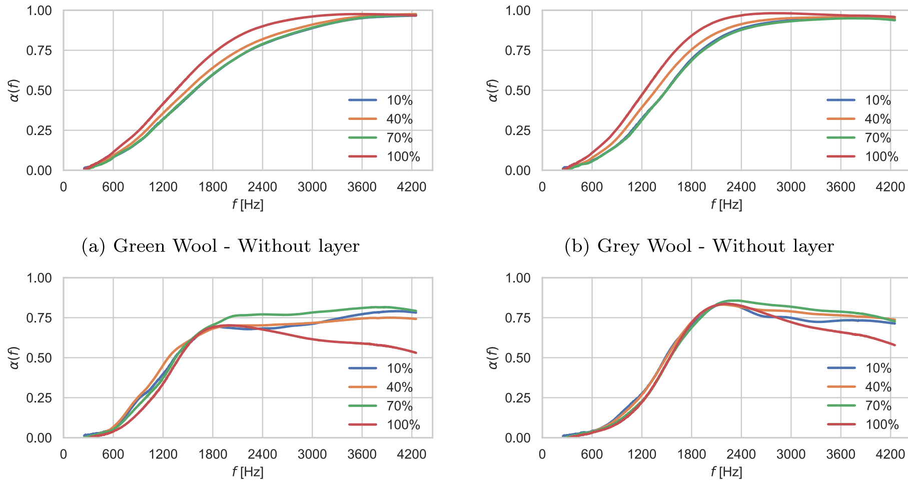

(a) Green Wool - Without layer

(b) Grey Wool - Without layer

(c) Green Wool - With layer

(d) Grey Wool - With layer

Fig. 8. Comparison of the effects of humidity levels on the sound absorption coefficient. Each curve represents the average of 27 measurements.

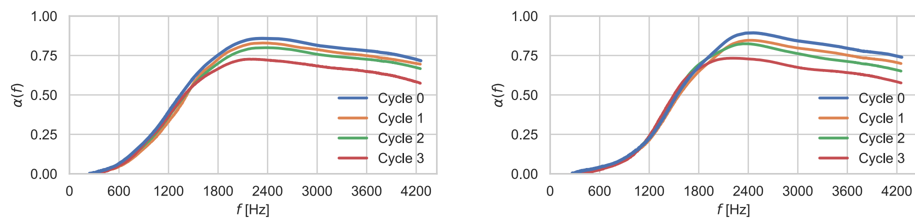

(a) Green Wool

(b) Grey Wool

Fig. 9. Comparison of the effects of repeated humidity cycling on the sound absorption coefficient. Each curve represents the average of 9 measurements.

The Fig. 4(c) and (d) report the behavior of specimens with the protective layer. Similarly to the previous specimens, the same installation-dependent trend is observed, although with different frequency distributions. As shown in Fig. 4(c), the sound absorption coefficient corresponding to the manual installation condition increases up to approximately 2200 Hz, beyond which a plateau region is observed. In contrast, the plunger-mounted configurations exhibit a downward-right shift of the absorption curves, with maximum absorption coefficients of approximately 0.78, 0.75 and 0.71 at around 2600 Hz for the *uniform*, *local* and *finger pressure* configurations, respectively. The largest variability among the plunger-based configurations is observed within the 1800–3000 Hz range, where the difference between the two extreme configurations reaches approximately 22%. A similar, although less pronounced, behavior is observed for grey wool in Fig. 4(d), where an average variation of approximately 16% is visible within the narrower 2000–3000 Hz frequency range.

Overall, the results consistently indicate that the manual installation condition leads to higher sound absorption coefficients and to the occurrence of the absorption peak at lower frequencies compared to the plunger-based configurations. This behavior suggests that the mounting fixture may induce higher specimen compression, reducing the effective thickness and locally modifying the porous microstructure through pore closure effects, thereby decreasing the overall acoustic absorption performance. Furthermore, the progressively lower absorption observed from the *uniform* to the *localized* and *finger pressure* configurations may indicate that increasingly concentrated contact pressures promote more pronounced local microstructural alterations during mounting.

Fig. 8 shows the effect of four relative humidity levels: 10%, 40%, 70% and 100%. The Fig. 5(a) and (b) correspond to specimens without the protective layer. In both cases, sound absorption coefficient variations between humidity levels are observed in the 600-3600 Hz frequency band. The aforementioned Fig. 5(a) and (b) have maximum average differences in percentage between the most distant curves, of approximately 22% for green wool and 26% for grey wool. Despite these variations, the asymptotic convergence to $\alpha \approx 0.98$ for green wool and $\alpha \approx 0.92$ for grey wool is preserved for all humidity conditions. The Fig. 5(c) and (d) correspond to specimens equipped with the protective layer. In both cases, variations of the sound absorption coefficient curves between humidity levels can be observed in the low and high frequency bands. The presence of the protective layer modifies the overall spectral shape, introducing characteristic stationary points around 1720 Hz for green wool and 2020 Hz for grey wool. The aforementioned Fig. 5(c) and (d) exhibit average differences in percentage between the most distant curves of approximately 17% before and 31% after the stationary point for green wool and about 8% before and 26% after the stationary point for grey wool.

The *Humidity Cycling Degradation Dataset* $\mathcal{D}_2$ reports the sound absorption coefficient curves, averaged over 9 measurements, for the two glass wool materials with the protective layer, in order to isolate the effects of repeated humidity cycling. Fig. 9 illustrates the influence of four humidity cycles: cycle 0, cycle 1, cycle 2 and cycle 3. The Fig. 6(a) refers to green wool. Differences among cycles are primarily observed in the 1800–4250 Hz frequency band. The average differences in percentage between two consecutive moisture cycles amount to approximately 5% from cycle 0 to cycle 1, about 3% from cycle 1 to cycle 2 and 13% from cycle 2 to cycle 3 (with higher deviations in the high frequency band). The Fig. 6(b) corresponds to grey wool and exhibits variations within the same frequency band (1800–4250 Hz). The averaged differences between successive cycles for the grey wool are approximately 4% from cycle 0 to cycle 1, 3% from cycle 1 to cycle 2 and 15% from cycle 2

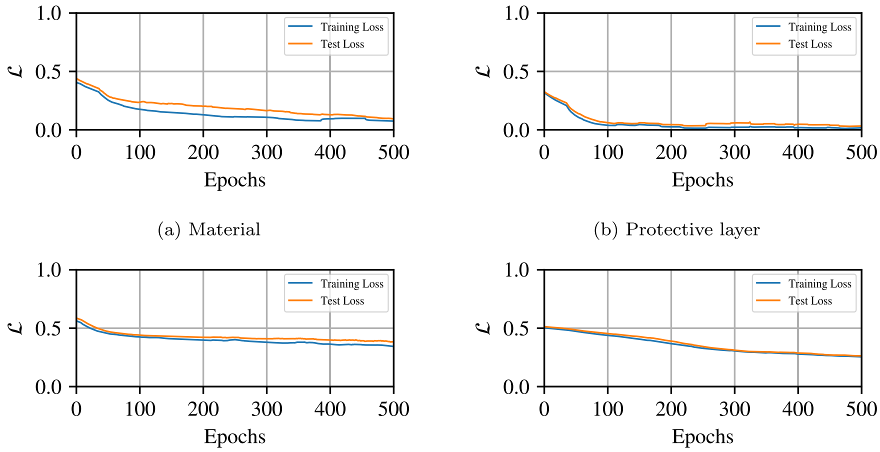

(a) Material (b) Protective layer (c) Installation (d) Relative humidity

Fig. 10. Univariate cross-entropy loss $\mathcal{L}$ for the features in dataset $\mathcal{D}_1$. Training and test losses are shown in blue and Orange, respectively.

Table 3
Classification accuracy of the univariate and multivariate ANN methods for the categorical features in dataset $\mathcal{D}_1$.

	Material	Protective Layer	Installation	Humidity Level
Values: $\mathbb{E}[f_k(\mathbf{x})]$	Green Wool: 50.0 Grey Wool: 50.0	With: 50.0 Without: 50.0	Uniform p.: 25.0 Localized p.: 25.0 Finger p.: 25.0 Manual p.: 25.0	10%: 25.0 40%: 25.0 70%: 25.0 100%: 25.0
Accuracy (in %)				
Univariate $\mathcal{M}_1$	96.0 ± 2.05	99.5 ± 0.37	57.9 ± 3.72	69.6 ± 3.83
Multivariate $\mathcal{M}_2$	94.5 ± 5.00	99.5 ± 0.00	46.6 ± 5.00	72.3 ± 5.00

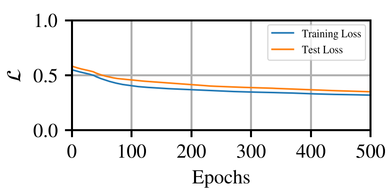

Fig. 11. Multivariate cross-entropy loss $\mathcal{L}$ for dataset $\mathcal{D}_1$. Training and test losses are shown in blue and Orange, respectively.

to cycle 3 (with higher deviations in the mid-frequency band). In both materials, a recursive decay of acoustic performance is observed as the number of applied humidity cycles increases.

4.2. Dataset $\mathcal{D}_1$: classification results

The *univariate* cross-entropy loss trends are reported in Fig. 10. The *univariate* classification accuracies reported in Table 3, provide a quantitative assessment of the predictive performance for each categorical feature. In particular, Table 3 reports both the baseline accuracy, given by the expected value $\mathbb{E}[f_k(\mathbf{x})]$ and the corresponding accuracy per feature. The observed decrease in both training and test loss, together with their subsequent stabilization at low values (see Fig. 10), suggests that the algorithm successfully captures the relationships governing the acoustic response of the analyzed configurations. The *multivariate* cross-entropy loss evolution over the training epochs is reported in Fig. 11, confirming a stable convergence behavior for both training and test sets.

Table 3 quantitatively corroborates the aforementioned cross-entropy loss trends. For the *material* and *protective layer* features, both $\mathcal{M}_1$ and $\mathcal{M}_2$ achieve accuracies largely exceeding the corresponding expected value (50%), reaching values above 94% and 99%, respectively. A different behavior is observed for the *installation* condition. Since four mounting values are considered, the expected random classification accuracy corresponds to 25%. The *univariate* $\mathcal{M}_1$ method achieves an accuracy of 57.9%, whereas the *multivariate* $\mathcal{M}_2$ reaches 46.6%. Consistent with the decreasing training and test loss trends, these results indicate that the algorithm is capable of identifying installation-dependent acoustic signatures for the majority of the analyzed cases. The observed classification capability is likely associated with the marked differences between manual and plunger-based mounting conditions, which constitute the dominant source of variability within the installation values. Similar to *material* and *protective layer* features, is the behavior for the *humidity level*. The *univariate* $\mathcal{M}_1$ method achieved an accuracy of 69.6% while the *multivariate* $\mathcal{M}_2$ reached 72.3%; both significantly above the 25% random baseline. The *multivariate* approach achieves classification accuracies comparable to those obtained through the corresponding *univariate* analyses. Since $\mathcal{M}_2$ simultaneously learns all the experimental factors, a substantial increase in performance with respect to $\mathcal{M}_1$ would suggest the presence of strong coupled or non-linear interactions among the investigated variables. However, the comparable accuracies observed for *material*, *protective layer* and *installation*, together with the only marginal improvement obtained for the *humidity level*, indicate that the dominant acoustic signatures associated with each factor remain largely distinguishable and weakly coupled within the analyzed dataset.

4.3. Dataset $\mathcal{D}_2$: classification results

The *univariate* and *multivariate* cross-entropy loss trends of dataset $\mathcal{D}_2$ are reported in Figs. 12 and 13, respectively. In both cases, the training and test losses decrease during the initial training stages and subsequently converge toward stable plateau values.

For performance evaluation, the model corresponding to the minimum test loss is retained. Training is extended up to 1000 epochs to verify whether additional improvements can be achieved after convergence; however, no significant gains in classification performance are observed beyond the early training stages.

Table 4 reports the classification accuracies obtained for the categorical features of dataset $\mathcal{D}_2$ (see Table 2). The *material* feature is reliably classified by both methods, with accuracies exceeding 91%. This indicates that the presence of the protective layer, which is fixed in dataset $\mathcal{D}_2$, does not influence the *multivariate* material classification.

Regarding the classification of the *humidity cycles*, the *univariate* method $\mathcal{M}_1$ achieves an accuracy of 82.5%, while the *multivariate* method

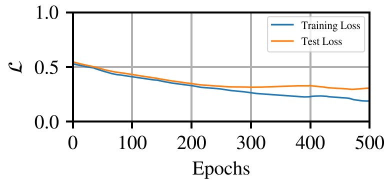

Fig. 12. Univariate cross-entropy loss $\mathcal{L}$ for the humidity cycle feature in dataset $\mathcal{D}_2$. Training and test losses are shown in blue and Orange, respectively.

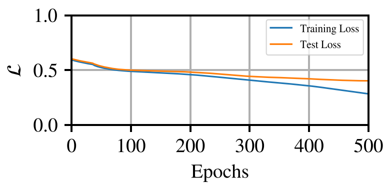

Fig. 13. Multivariate cross-entropy loss $\mathcal{L}$ for dataset $\mathcal{D}_2$. Training and test losses are shown in blue and Orange, respectively.

Table 4
Classification accuracy of the univariate and multivariate ANN methods for the categorical features in dataset $\mathcal{D}_2$.

	Material	Humidity Cycles	Specimen
Values: $\mathbb{E}[f_k(\mathbf{x})]$	Green Wool: 50.0 Grey Wool: 50.0	Cycle 0: 25.0 Cycle 1: 25.0 Cycle 2: 25.0 Cycle 3: 25.0	Specimen 1: 33.3 Specimen 2: 33.3 Specimen 3: 33.3
Accuracy (in %)			
Univariate $\mathcal{M}_1$	92.2 ± 5.66	82.5 ± 6.33	42.2 ± 7.10
Multivariate $\mathcal{M}_2$	91.5 ± 8.50	70.0 ± 17.5	37.0 ± 13.3

$\mathcal{M}_2$ exhibits greater variability, as indicated by the higher standard deviation.

The identification of individual *specimens* is included to assess whether nominally identical samples exhibit distinguishable responses under repeated humidity cycles, potentially due to non-uniform moisture impregnation within the porous structure. In this context, classification performance significantly above the random baseline (33.3%) would indicate specimen-dependent effects induced by the humidification process.

The obtained accuracies are 42.2% for $\mathcal{M}_1$ and 37.0% for $\mathcal{M}_2$. Although slightly above the random level, both values remain close to baseline performance, suggesting that no consistent specimen-specific signatures emerge across humidity cycles. This indicates that the humidification process is repeatable for both the studied glass wool materials.

4.4. Datasets $\mathcal{D}_1$ and $\mathcal{D}_2$: interpretability results

The interpretability analysis for both datasets $\mathcal{D}_1$ and $\mathcal{D}_2$ is performed using SHAP values computed on the *univariate* method $\mathcal{M}_1$. The *univariate* formulation is adopted to isolate the influence of each categorical feature and to identify the frequency bands that most strongly affect the sound absorption coefficient curves for the specific feature under investigation.

Regarding dataset $\mathcal{D}_1$, Fig. 14 reports the frequency-dependent SHAP values for the *installation* and *humidity level* features.

The class-specific SHAP value $\phi_k^{(l)}(f_r)$ is defined by Eq. (10), while the total absolute SHAP contribution $\Phi_{i,j}^{(l)}(f_r)$ and the associated relevance criterion are defined in Eqs. (12)–(14) (Section 3.4). The solid curves in Figs. 14 and 15 represent the mean $\mu_{i,j}(f_r)$ of $\Phi_{i,j}^{(l)}(f_r)$ over the analyzed curves, while the shaded regions represent the corresponding interval $\mu_{i,j}(f_r) \pm \sigma_{i,j}(f_r)$.

For the installation configuration, shown in Fig. 14(a), the frequency components satisfying Eq. (14) are primarily concentrated in a dominant region below 1500 Hz, with the largest contributions occurring between approximately 800 and 1200 Hz and an additional localized maximum around 1400 Hz. Weaker and more localized contributions are observed between 2000 and 2400 Hz. This second region coincides with the interval in which the preliminary analysis (see Section 4.1) revealed pronounced installation-dependent differences, confirming that it contains relevant information for distinguishing the investigated mounting configurations.

From a physical perspective, mounting pressure can simultaneously modify the effective specimen thickness, local fibre density and airflow resistivity [5]. Non-uniform and manual mounting can additionally produce spatially heterogeneous compression and variations in the specimen tube contact condition. The combined action of these mechanisms is consistent with the dominant low frequency SHAP contributions and the more localized contributions observed at higher frequencies, rather than with a uniform modification of the absorption coefficient over the entire investigated spectrum.

The SHAP contributions associated with the *relative humidity* feature are reported in Fig. 14(b). The frequency components satisfying Eq. (14) are primarily concentrated in three spectral regions: (i) the low frequency region below approximately 1500 Hz, (ii) the mid-frequency region between approximately 2200 and 3200 Hz and (iii) the high frequency region above approximately 3600 Hz. Comparatively lower contributions are observed between approximately 1500 and 2200 Hz and between 3200 and 3600 Hz. In the high frequency region, the SHAP contribution increases progressively toward the upper limit of the investigated frequency range.

Moisture uptake may modify the air-filled pore space and the interaction between the air and the fibre surfaces, thereby affecting the effective airflow resistivity and the viscous and thermal dissipation mechanisms within the porous structure [12,13]. In fibrous porous absorbers, acoustic energy is dissipated mainly through viscous and thermal losses generated by the oscillatory motion of air within the

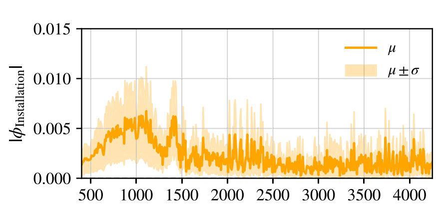

(a) Installation

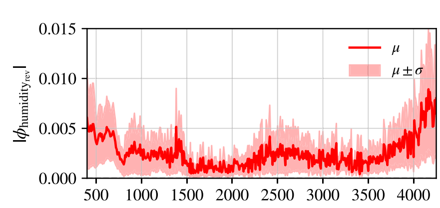

(b) Relative humidity

Fig. 14. Frequency-dependent total absolute SHAP contributions obtained from the *univariate* method $\mathcal{M}_1$ for the installation and relative-humidity features of dataset $\mathcal{D}_1$. Solid curves denote μ, while the shaded regions represent $\mu \pm \sigma$.

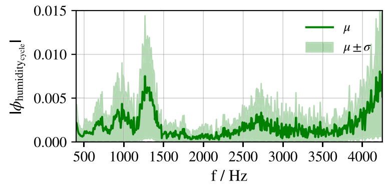

Fig. 15. Frequency-dependent total absolute SHAP contributions obtained from the *univariate* method $\mathcal{M}_1$ for the humidity-cycle feature of dataset $\mathcal{D}_2$. The solid curve denotes μ, while the shaded region represents $\mu \pm \sigma$.

interconnected pores. Moisture adsorbed on the fibre surfaces or retained within the porous network may modify the effective airflow paths and, consequently, the acoustic impedance and dissipative response of the material [12,13]. Since these properties are frequency dependent, moisture exposure can produce non-uniform variations in the sound absorption coefficient across the investigated spectrum, consistent with the separated regions identified by the SHAP analysis. However, because moisture distribution and acoustic transport parameters were not measured independently, the present results do not allow a distinct physical mechanism to be assigned to each frequency region.

Regarding dataset $\mathcal{D}_2$, Fig. 15 shows the total absolute SHAP contribution associated with the *humidity cycle* feature. The frequency components satisfying Eq. (14) are mainly concentrated in the low frequency region, with a distinct maximum between approximately 1200 and 1400 Hz, and in the high frequency region above approximately 3600 Hz. A weaker and broader contribution remains visible between approximately 2500 and 3000 Hz. Thus, the low and high frequency regions provide the greatest discriminative information for identifying the number of humidity cycles, whereas the mid-frequency contribution is less pronounced than that observed for the relative-humidity feature in dataset $\mathcal{D}_1$.

The correspondence between the low and high frequency regions identified in the two datasets indicates that relative humidity and repeated moisture exposure produce distinguishable acoustic signatures in common portions of the frequency spectrum.

5. Conclusions

The acoustic response of two aeronautical glass wools has been analyzed through a framework combining impedance tube measurements, supervised classification based on *univariate* and *multivariate* neural network methods and SHAP-based explainability analyses. Within this approach, the classification task serves as a qualitative discriminator to determine whether a given categorical feature leaves a detectable signature in the sound absorption coefficient, while SHAP values quantify the spectral contribution of each feature. For the *Installation and Environmental Variability Dataset* $\mathcal{D}_1$, material type and protective layer are identified as the most discriminative features, with classification accuracies exceeding 94% and 99%, respectively.

With specific regard to the installation factor, the proposed framework reveals clear and structured variations in the sound absorption coefficient across the investigated mounting conditions. Plunger-based configurations produce noticeable spectral changes, with differences of about 16–22% depending on the material and frequency range. In contrast, manual installation leads to higher absorption values and a shift of the peak response toward lower frequencies, a trend observed across all cases. This is also reflected in the classification results, where the *univariate* model reaches 57.9% accuracy and the *multivariate* model 46.6%, compared to a 25% random baseline. These values indicate that installation effects are present and detectable. In agreement with this, the SHAP analysis shows that the most relevant contributions are concentrated in two frequency regions, rather than being spread uniformly across the spectrum. From a physical point of view, the observed behavior is mainly driven by how the contact pressure is distributed at the specimen–fixture interface. The plunger-based configurations, which promote a more uniform pressure field, tend to preserve a more consistent acoustic response. Conversely, more localized contact conditions can lead to partial pore closure, local compaction and damaging of the fibrous structure. In this sense, the use of a plunger-based mounting system improves repeatability by ensuring a more controlled and reproducible contact condition, while the uniform pressure termination in particular helps mitigate the aforementioned physical effects that have been shown to introduce variability in the measurements.

Relative humidity has a significant influence on the sound absorption coefficient, producing variations between 17-31% depending on the adopted configuration and classification accuracies around 70%. SHAP-based analysis revealed that these humidity-related effects are frequency dependent, with the highest sensitivity in three bands: (i) below 1300 Hz, (ii) between 2200 and 3200 Hz and (iii) above 3600 Hz. For the *Humidity Cycling Degradation Dataset* $\mathcal{D}_2$, repeated humidity cycles progressively modified the sound absorption coefficient response. Variations between consecutive cycles ranged from a few percent in the initial stages to approximately 10-15% in later cycles. The classification framework captured these changes with accuracies up to 85%. Limited discriminability among nominally identical specimens suggests that the observed acoustic variations induced by humidity cycles are broadly consistent across samples. Overall, the proposed framework demonstrates how experimental impedance tube measurements combined with machine learning classification and SHAP-based explainability can identify features and frequency bands governing the variability of the sound absorption coefficient of aeronautical glass wool materials. The proposed methodology is inherently data-driven and can be transferred to other experimental campaigns involving different features and values.

Future research may extend the present investigation to additional porous materials, material parameters (such as flow resistivity) and specimen thickness. The methodology may also be transferred from impedance-tube measurements to reverberation-chamber testing in order to investigate full-scale insulation blankets under more realistic operating conditions.

CRediT authorship contribution statement

Alfonso Caiazzo: Writing – review & editing, Writing – original draft, Methodology, Data curation, Conceptualization. **Giuseppe Petrone:** Supervision, Data curation. **Alessandro Casaburo:** Supervision. **Immacolata Climaco:** Data curation. **Aurelio Bifulco:** Supervision.

Declaration of competing interest

The authors declare that they have no known competing financial interests or personal relationships that could have appeared to influence the work reported in this paper.

Acknowledgements

The authors gratefully acknowledge BCs Salvatore and Ida for their support during the experimental campaign. The authors further express their sincere gratitude to Eng. Bonaventura Vitolo (GEVEN S.p.A.) for his valuable support and for providing the samples used in this research.

Data availability

Research link provided.

References

[1] Pennig S, Quehl J, Rolny V. Effects of aircraft cabin noise on passenger comfort. Ergonomics 2012;55(10):1252–65. https://doi.org/10.1080/00140139.2012.703698
[2] Federal Aviation Administration. Aircraft materials fire test handbook. Washington, DC: U.S. Department of Transportation, FAA; 2000, DOT/FAA/AR-00/12.
[3] Latsuzbaya V, Middendorf P, Völkle D, Weber C. Improving the thermal properties of aircraft cabin interiors with the integration of vacuum insulation panels. CEAS Aeronaut J 2022;13(3):705–18. https://doi.org/10.1007/s13272-022-00590-6

[4] Nazari S, Ivanova TA, Mishra RK, Muller M. A review focused on 3D hybrid composites from glass and natural fibers used for acoustic and thermal insulation. J Compos Sci 2025;9(8):448. https://doi.org/10.3390/jcs9080448

[5] Petrone G, Sorrentino A, De Bono E, Polito T, Marulo F, et al. Installation effects on sound absorption and flow resistivity of glass wool fibres. In: Proceedings of ISMA 2018-international conference on noise and vibration engineering and USD 2018-international conference on uncertainty in structural dynamics. KU Leuven-Departement Werktuigkunde; 2018. p. 721–33.

[6] Ikpekha OW, Simms M. Effect of acoustic absorber type and size on sound absorption of porous materials in a full-scale reverberation chamber. In: Acoustics, vol. 7. MDPI; 2025. p. 3. https://doi.org/10.3390/acoustics7010003

[7] Stender M, Adams C, Wedler M, Grebel A, Hoffmann N. Explainable machine learning determines effects on the sound absorption coefficient measured in the impedance tube. The journal of the Acoustical Society of America 2021;149(3):1932–45. https://doi.org/10.1121/10.0003755

[8] Stanley DR. Impedance tube specimen preparation and mounting issues. In: INTER-NOISE and NOISE-CON congress and conference proceedings, 2012. Institute of Noise Control Engineering; 2012. p. 9126–32.

[9] Koruk H. An assessment of the performance of impedance tube method. Noise Control Eng J 2014;62(4):264–74.

[10] Gibson P, Rivin D, Kendrick C, Schreuder-Gibson H. Humidity-dependent air permeability of textile materials1. Text Res J 1999;69(5):311–7. https://doi.org/10.1177/004051759906900501

[11] Jeon C-K, Lee J-S, Chung H, Kim J-H, Park J-P. A study on insulation characteristics of glass wool and mineral wool coated with a polysiloxane agent. Adv Mater Sci Eng 2017;2017(1):3938965. https://doi.org/10.1155/2017/3938965

[12] Marmoret L, Collet F, Beji H. Moisture adsorption in glass wool products. High Temperatures-High Pressures 2011;40(1):31–46.

[13] Yilmazer S, Ozdeniz MB. The effect of moisture content on sound absorption of expanded perlite plates. Build Environ 2005;40(3):311–8. https://doi.org/10.1016/j.buildenv.2004.07.004

[14] Zhao K, Liu Y, Du J. A novel Fourier series-neural network hybrid approach for the boundary supporting stiffness identification of a flexible beam. J Mech Sci Technol 2023;37(6):2727–40.

[15] Du J, Zhao K, Liu Y, Wang Y, Zhong X. Acoustic cavity boundary impedance identification based on hybrid neural network and boundary-smoothed Fourier series method. J Vib Eng Technol 2025;13(1):65.

[16] Casaburo A, Petrone G, Franco F, De Rosa S. Characterization of porous materials with artificial neural networks. The Journal of the Acoustical Society of America 2025;157(2):980–92.

[17] Bianco MJ, Gerstoft P, Traer J, Ozanich E, Roch MA, Gannot S, Deledalle C-A. Machine learning in acoustics: theory and applications. The Journal of the Acoustical Society of America 2019;146(5):3590–628.

[18] Johns Manville. Microlite AA blankets: aircraft thermal and acoustic insulation. Johns Manville, Product data sheet, 2020. https://www.jm.com/content/dam/jm/global/en/oem/aerospace/microlite-aa/JM_Microlite_AA_Data_Sheet.pdf [accessed 28 July 2026].

[19] Lamart Corporation. LAMAGUARD-400HR: film for thermal and acoustic insulation. Lamart Corporation, Product data sheet, 2026. https://lamartcorp.com/products/orcon-products/films-orcofilm/lamaguard-400hr/ [accessed 28 July 2026].

[20] Ando Y, Kosaka K. Effect of humidity on sound absorption of porous materials. Appl Acoust 1970;3(3):201–6. https://doi.org/10.1016/0003-682X(70)90024-1

[21] Adams C, Grebel A, Wenzel S, Schoder S, Kaltenbacher M. FOAM 01: acoustic material; Jan, 2024. https://doi.org/10.5281/ZENODO.10551343

[22] International Organization for Standardization. ISO 10534-2:2023(E) acoustics - determination of sound absorption coefficient and impedance in impedance tubes - Part 2: Two-microphone technique for normal sound absorption coefficient and normal surface impedance; 2023.

[23] E33 Committee. ASTM E1050-19 test method for impedance and absorption of acoustical materials using a tube, two microphones and a digital frequency analysis system; 2019. https://doi.org/10.1520/E1050-19

[24] Potdar K, Pardawala TS, Pai CD. A comparative study of categorical variable encoding techniques for neural network classifiers. Int J Comput Appl 2017;175(4):7–9.

[25] Caiazzo A, Petrone G, Kraxberger F, Adams C, De Rosa S, Franco F. Comparing explainable machine learning methods to determine uncertainty factors of sound absorption coefficient measurements with an impedance tube. Noise and Vibration: Emerging Methods NOVEM2025 Garmisch – Partenkirchen May 2025;6–8.

[26] Salehi S, Kavgic M, Bonakdari H, Begnoche L. Comparative study of univariate and multivariate strategy for short-term forecasting of heat demand density: exploring single and hybrid deep learning models. Energy AI 2024;16:100343. https://doi.org/10.1016/j.egyai.2024.100343

[27] Stender M, Wedler M, Hoffmann N, Adams C. Explainable machine learning: a case study on impedance tube measurements. In: INTER-NOISE and NOISE-CON congress and conference proceedings, vol. 263. Institute of Noise Control Engineering; 2021. p. 3223–34. https://doi.org/10.3397/IN-2021-2342

[28] Okewu E, Misra S, Lius F-S. Parameter tuning using adaptive moment estimation in deep learning neural networks. In: Computational science and its Applications–ICCSA 2020: 20th international conference, Cagliari, Italy, July 1–4, 2020, proceedings, Part VI 20. Springer; 2020. p. 261–72.

[29] Plath N, Toussaint M, Nakajima S. Multi-class image segmentation using conditional random fields and global classification. In: Proceedings of the 26th annual international conference on machine learning; 2009. p. 817–24. https://doi.org/10.1145/1553374.1553479

[30] Dmitriev K, Kaufman AE. Learning multi-class segmentations from single-class datasets. In: Proceedings of the IEEE/CVF conference on computer vision and pattern recognition; 2019. p. 9501–11.

[31] Anjum MA, Amin J, Sharif M, Khan HU, Malik MSA, Kadry S. Deep semantic segmentation and multi-class skin lesion classification based on convolutional neural network. IEEE Access 2020;8:129668–78. https://doi.org/10.1109/ACCESS.2020.3009276

[32] Lundberg S. A unified approach to interpreting model predictions, arXiv preprint arXiv:1705.07874. 2017.

[33] Sundararajan M, Najmi A. The many Shapley values for model explanation. In: International conference on machine learning. PMLR; 2020. p. 9269–78.

[34] Hogan M, Aouf N, Spencer P, Almond J. Explainable object detection for uncrewed aerial vehicles using kernelshap. In: 2022 IEEE international conference on autonomous robot systems and competitions (ICARSC). IEEE; 2022. p. 136–41.

[35] Caiazzo A, Kraxberger F, Petrone G, De Rosa S, Adams C. Identifying sources of variability in impedance tube sound absorption measurements with multivariate explainable machine learning. J Sound Vib 2026;120003.

[36] Caiazzo A, Kraxberger F, Adams C, Wurzinger A, Petrone G, Schoder S, De Rosa S, Kaltenbacher M. FOAM 02: acoustic material; 2025. https://doi.org/10.5281/zenodo.14190550

[37] Genuer R, Poggi J-M, Tuleau-Malot C. Variable selection using random forests. Pattern Recognit Lett 2010;31(14):2225–36.